Confinement of gigahertz sound and light in Tamm plasmon resonators

V. Villafañe,[1] A. E. Bruchhausen,[1] B. Jusserand,[2] P. Senellart,[3,4] A. Lemaître,[3] and A. Fainstein[1,*]
[1]*Centro Atómico Bariloche & Instituto Balseiro, C.N.E.A., 8400 San Carlos de Bariloche, Río Negro, Argentina*
[2]*Institut des NanoSciences de Paris, UMR 7588 C.N.R.S. - Université Pierre et Marie Curie, 75015 Paris, France*
[3]*Laboratoire de Photonique et de Nanostructures, C.N.R.S., 91460 Marcoussis, France*
[4]*Département de Physique, Ecole Polytechnique, F-91128 Palaiseau, France*
(Received 29 July 2015; published 9 October 2015)

We demonstrate theoretically and by pump-probe picosecond acoustics experiments the simultaneous confinement of light and gigahertz sound in Tamm plasmon resonators, formed by depositing a thin layer of Au onto a GaAs/AlGaAs Bragg reflector. The cavity has InGaAs quantum dots (QDs) embedded at the maximum of the confined optical field in the first GaAs layer. The different sound generation and detection mechanisms are theoretically analyzed. It is shown that the Au layer absorption and the resonant excitation of the QDs are the more efficient light-sound transducers for the coupling of near-infrared light with the confined acoustic modes, while the displacement of the interfaces is the main back-action mechanism at these energies. The prospects for the compact realization of optomechanical resonators based on Tamm plasmon cavities are discussed.

DOI: 10.1103/PhysRevB.92.165308 PACS number(s): 63.22.−m, 78.30.Fs, 78.30.−j, 78.67.Pt

I. MOTIVATION

Optical Tamm plasmons are modes localized at the interface between a dielectric Bragg reflector (DBR) and a metal layer (typically Au or Ag) [1]. As compared to plasmon resonances of standard metal layers, optical Tamm plasmons have the benefit of reduced dissipation, and the direct coupling with light at normal incidence. Tamm plasmon resonators can also be considered as an asymmetric optical cavity, with some benefits and limitations with respect to standard DBR microcavities. As a limitation, there exists an intrinsic upper limit for the resonator Q factor (of a few 10^3 for Au) due to unavoidable losses in the metal layer. Advantages on the other hand are several: (1) easy fabrication, (2) the interesting possibility to confine laterally the optical mode by structuring only the metallic part [2], and (3) the possibility to reduce the associated damage on embedded emitters that typically arises with the lateral patterning into pillars. Tamm plasmon resonators have been proposed in recent years as attractive candidates for the development of efficient optical switches [3], innovative lasers [4,5], single-photon emitters [6], and cavity-polariton devices [7]. 3D optical confinement due to confined Tamm plasmons under metallic microdisks has been demonstrated, with both acceleration and inhibition of the spontaneous emission of single quantum dots (QDs) [2].

It is the purpose of this paper to analyze the potentiality of Tamm plasmon resonators in the domain of cavity optomechanics [8–11], namely, to demonstrate whether high-frequency vibrations and photons can be simultaneously confined in the same space, and be made to strongly interact, in these hybrid metal-semiconductor cavities. Light-induced rigidity, optomechanical cooling down to the quantum ground state of mechanical motion [12–15], and optomechanical self-oscillation [16,17] are some of the demonstrated striking consequences of so-called dynamical back-action in the domain of cavity optomechanics. If the appropriate conditions are met, Tamm resonators could be a quite rugged and compact implementation of these physics, with the potentiality for the coupling to optoelectronic phenomena, and ease of 3D confinement in wavelength dimensions using metallic disks.

In the domain of phononics, optical microcavities have been studied for strongly enhanced Raman spectroscopy of phonons [18–21] and as a means to amplify either the phonon generation, the detection, or both in picosecond acoustics experiments [22,23]. Along these lines it has been also recently shown [24] that GaAs/AlAs optical microcavities constitute at the same time optimized resonators for near-infrared light and for GHz-THz acoustic vibrations [25]. Simultaneous phonon-photon confinement has been demonstrated in these devices, with the possibility to selectively launch cavity breathing modes with direct laser pulse excitation of the structure [24,26,27]. In microcavities with photons and excitons in the strong-coupling regime, it has been also shown that this scheme of direct laser excitation enables the access to enormously enhanced optomechanical coupling of resonant (polariton mediated) photoelastic nature [28]. The dynamics of microcavities can be also driven by the external injection of acoustic pulses, either using quasimonochromatic surface acoustic waves [29,30] or bulk propagating broadband strains induced by femtosecond laser excitation of metal transducers [31–34].

Our aim here is to theoretically evaluate the potentiality of Tamm plasmon resonators for simultaneous acoustic phonon confinement, and to experimentally study the vibrational response of these structures by *direct* laser excitation using picosecond laser pulses resonantly tuned with the confined optical Tamm mode, and with the electronic transitions associated with a layer of embedded QDs. A theoretical modeling of the picosecond acoustics response is also presented, including a quantitative analysis of the different coherent phonon generation and detection mechanisms involved.

II. PHONON CONFINEMENT IN TAMM PLASMON RESONATORS

To analyze the simultaneous optical and acoustic confinement in Tamm plasmon resonators we consider similar

*afains@cab.cnea.gov.ar

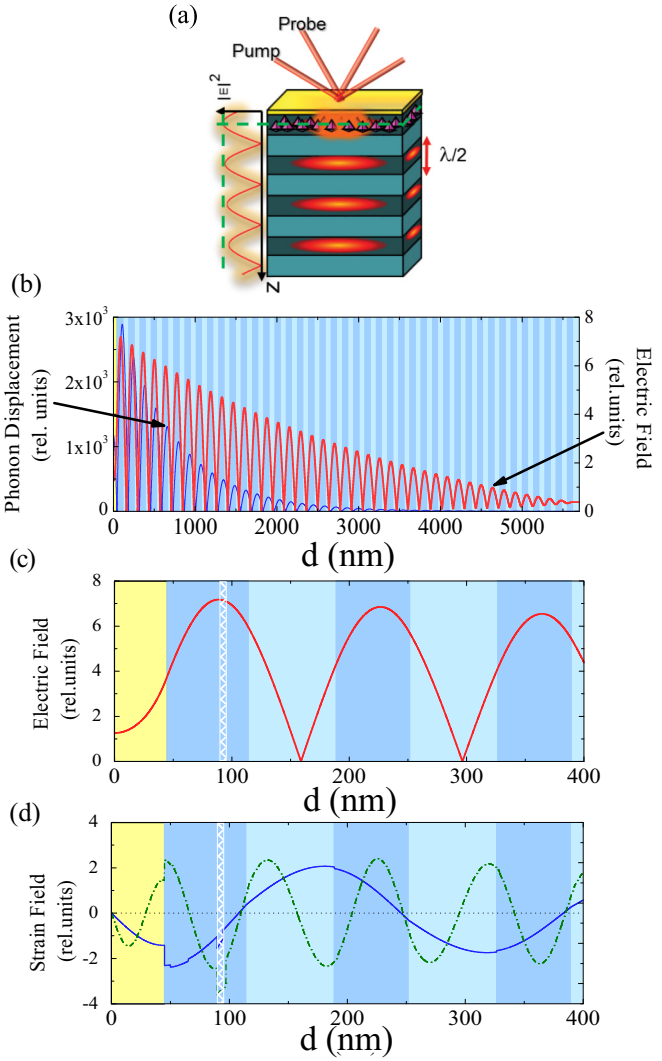

FIG. 1. (Color online) (a) Schematic diagram of the planar Tamm plasmon resonator with embedded QDs localized at the maximum of the confined optical field. (b) Amplitude of the electromagnetic field E (red curve) and lattice displacement u (blue curve) for the first confined optical and acoustic phonon modes, respectively. The calculation assumes incidence from the substrate (air side) of amplitude 1 for the acoustic (optical) case. (c) Detail of the electromagnetic field E corresponding to the Tamm optical mode. (d) Strain distribution (du/dz) corresponding to the first (20 GHz, solid) and third (60 GHz, dash-dotted) order acoustic confined modes.

structures to the ones designed for the demonstration of single-photon emission [2]. A DBR with 40 pairs of $\lambda/4n$ layers of $Al_{0.95}Ga_{0.05}As$ and GaAs was grown by molecular beam epitaxy, and 45 nm of gold were deposited on top of the DBR to complete the cavity [as illustrated with the scheme in Fig. 1(a)]. The first DBR layer after the metal is GaAs. A layer of self-assembled InGaAs QDs with high QD density was grown 45 nm below the surface, where the Tamm plasmon confined optical field is calculated to have a maximum [see Figs. 1(b) and 1(c)]. A 15 nm $Al_{0.2}Ga_{0.8}As$ layer is inserted between the QDs and the surface. This thin barrier allows isolating the QDs from surface defect states without modifying the intensity profile of the Tamm optical mode.

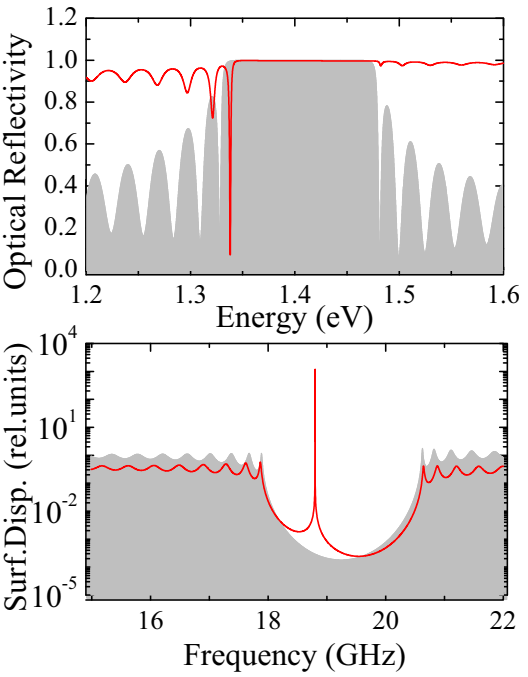

FIG. 2. (Color online) (a) Optical reflectivity as a function of wavelength (incidence of amplitude 1 from the air side) and (b) surface displacement as a function of frequency (incidence of amplitude 1 from the substrate side), for the bare DBR (shaded curves) and the Tamm resonator, that is, the same DBR with the added Au layer (red curves).

Standard transfer matrix formalisms were used to evaluate the optical reflectivity and electric field distribution, and the surface displacement and acoustic field distribution in the structure [35]. Published values were used for all required material parameters, complex index of refraction, sound velocity, and mass density. The surface displacement for a sound wave incident from the substrate is used to characterize the acoustic transmission through the structure (GHz vibrations do not propagate in air). Figure 2 presents these results for the Tamm structure using nominal thicknesses. Shaded curves correspond to the bare DBR, i.e., without the Au metal layer. The solid curves depict the complete Tamm plasmon resonator. The optical response shows the situation already treated in many papers, namely the typical oscillations of a DBR, with very high reflectivity within the so-called stop band, in this case ranging from 1.34 to 1.48 eV, and the strong change induced by the deposition of 45 nm of Au—namely, the overall increase of the reflectivity (characteristic of a Au mirror), the presence of oscillations due to interferences with the DBR, and most importantly, the appearance of a narrow resonance ($Q \sim 1300$) at the low-energy side of the stop band (≈ 1.34 eV in the figure), the so-called Tamm plasmon mode. The latter corresponds to a resonant confined mode, spatially localized at the surface and exponentially decaying into the DBR [Fig. 1(b)], with a maximum field approximately 45 nm below the DBR-Au interface [see Fig. 1(c)]. The optical response is smoothly dependent on the width of the metal layer, as illustrated with the color map in Fig. 3. Most notably, the Tamm resonance evolves from an edge mode into the optical

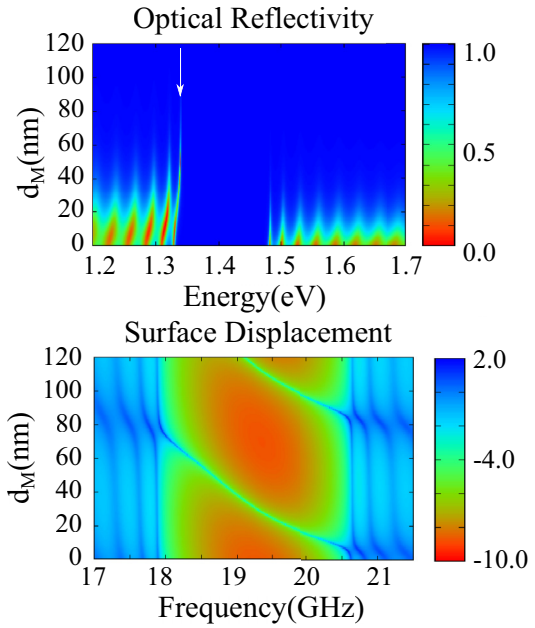

FIG. 3. (Color online) Color map corresponding to the optical reflectivity as a function of wavelength for incidence of amplitude 1 from the air side (a), and surface displacement as a function of frequency for incidence of amplitude 1 from the substrate side (b) for varying Au layer thickness of the Tamm resonator. The white arrow in (a) indicates the optical Tamm plasmon mode. Note that the displacement is presented in logarithmic scale.

gap, to rapidly stabilize its energy around 1.34 eV (indicated with a white arrow in the figure). The width of the mode decreases with increasing Au thickness, but the most important effect above 50 nm is a reduction of the associated dip, until it disappears above 100 nm because of light incident from the air side being fully reflected by the metal layer.

Particularly interesting is the analysis of the acoustic response of the same structure. As shown in Fig. 2, the DBR also performs as a quite efficient acoustic mirror [36–38], centered around 19.2 GHz, and ranging from 18 to 20.5 GHz (note the logarithmic scale in the figure). Moreover, the incorporation of the 45-nm-layer Au on top of the DBR leads to the appearance of a very narrow resonance quite well centered within the acoustic gap. The acoustic field spatial distribution corresponding to this resonant mode (which for simplicity we will call the Tamm acoustic mode), shown in Fig. 1(b), also corresponds to a mode localized at the surface and exponentially decaying into the DBRs. The steeper decay into the DBR as compared to the Tamm plasmon field reflects the much higher Q factor of the acoustic resonance. Most notably, the Tamm acoustic mode is a proper cavity-like mode as evidenced by its dependence on Au-layer thickness shown in Fig. 3. The Tamm acoustic mode develops from a mode associated with the metal layer, partially localized due to the strong acoustic mismatch between Au and the semiconductor materials [$Z_{Au} \approx 63 \times 10^6$ kg/(s m^2), while for all involved III-V materials $Z \approx (21\text{–}26) \times 10^6$ kg/(s m^2)]. This localized mode shifts with varying Au thickness, anticrosses with the higher density continuum states, and becomes strongly localized as it traverses the DBR stop band. In fact, it turns out to be well tuned within the DBR stop band for a Au thickness of 45 nm, a value chosen to optimize the optical properties of the resonator.

III. PICOSECOND ACOUSTICS EXPERIMENTS

Having shown theoretically that Tamm plasmon resonators also confine GHz acoustic vibrations in the same space, we proceed to their study by pump-probe differential reflectivity spectroscopy. Reflection-type pump-probe experiments [39] were performed at room temperature and at 80 K using a cold finger cryostat, with the laser energy tuned around the Tamm plasmon cavity mode. The latter depending on temperature was either slightly blueshifted from resonance (room temperature), or at resonance (80 K) with the QDs' absorption. Resonant coherent phonon generation experiments have been extensively used in the past for the study of layered semiconductor systems (see for example Refs. [40–42]) and for the selective excitation of confined acoustic vibrations in sound resonators [24,43]. They have also been specifically used to study the generation of phonons in embedded InAs QD layers similar to the ones included in the studied Tamm plasmon structure [44,45].

Picosecond pulses (∼1 ps, ∼920 nm, ∼1.348 eV) from a mode-locked Ti:sapphire laser, repetition rate 80 MHz, were split into cross-polarized pump (power around 20 mW) and probe (typically 2 mW) pulses. Photon pulses of 1 ps are chosen so that their spectral width is smaller than that of the Tamm plasmon resonance ($\Delta\lambda \sim 2$ nm). Both pulses were focused onto superimposed ∼50-μm-diameter spots. The optically resonant coupling of light to the microcavity was done as described in Refs. [46] and [47]. The probe is tuned close to normal incidence to the high-energy flank of the optical cavity mode. The pump pulse, at the same wavelength, is tuned resonant with the cavity mode. To this purpose a fine tuning of the pump pulse incidence angle is performed [22,46].

Figure 4 presents in its top panel the numerical Fourier transform of the picosecond acoustic traces acquired for 2 ns at room temperature. To help identify the modes the bottom panel shows the dispersion of folded acoustic phonons corresponding to the bare DBR. Note that acoustic stop bands open at the Brillouin zone edges, but not at zone center. Confined acoustic modes are thus to be expected at energies corresponding to odd numbers of the fundamental frequency at ≈19 GHz. As follows from the measured phonon spectra, peaks are indeed observed at energies corresponding to these confined Tamm acoustic modes, but also at zone-center vibrations. The insets in Fig. 4 show the calculated spatial distribution of the modes, highlighting the different nature of the two kinds of phonons: confined for the acoustic Tamm vibrations, extended throughout the DBRs for the zone-center modes. The explanation for the experimental observation of these two types of modes is, however, different. While a full theoretical calculation will be presented below, it is possible to understand this observation with simple symmetry arguments. Photon and phonon fields are confined in the same place of space, and it is this overlapping spatial confinement that explains the coupling of light with the confined acoustic Tamm modes. At the same time, the structure is essentially a finite-size periodic DBR. According to selection rules for

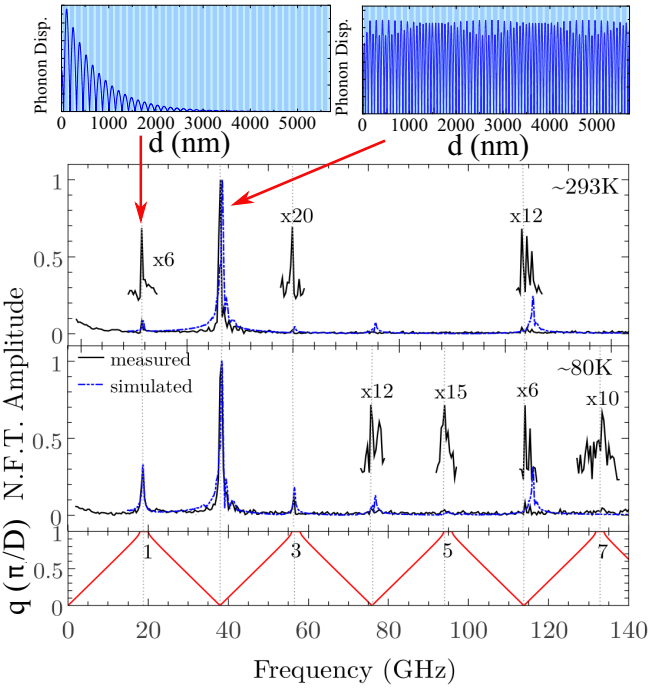

FIG. 4. (Color online) Amplitude of the numerical Fourier transform of picosecond acoustic traces taken with the laser resonant with the Tamm optical mode at room temperature (top) and 80 K (middle). Black curves are experimental; blue dash-dotted curves are the calculated spectra (see text for details). The bottom panel shows the corresponding dispersion of the folded acoustic phonons of the bare DBR. The top smaller panels show the calculated spatial distribution of the first observed zone edge (confined) and zone center (DBR-like) phonons.

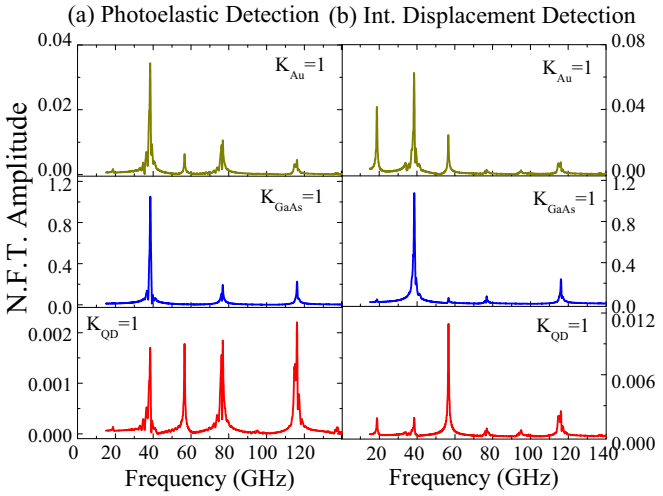

FIG. 5. (Color online) Calculated pump-probe spectra for different generation and detection mechanisms. The left (right) panels correspond to photoelastic (interface displacement) detection processes. Spectra are calculated with finite generation efficiency ($K = 1$) either in the Au layer, InGaAs QDs, or GaAs layers of the DBR (indicated in each panel), and 0 otherwise.

a periodic system, the optical generation of coherent phonons occurs for $q_G = 0$ (zone-center) vibrations, while the detection in back-scattering geometry is sensitive to $q_D = 2k$ modes (here q and k are the phonon and photon wave number, respectively) [22]. However, at resonance with the optical cavity mode, $k = \pi/d$, with d the DBR period. It follows that $q_D = 2\pi/d$, which has the same symmetry as a $q = 0$ mode. This implies that zone-center modes are generated and detected at the DBR.

To better understand the observed spectra we proceed now to its analysis with a full model for pump-prove differential reflectivity experiments, as previously described in Ref. [48]. Within this framework the coherent phonon generation process can be described as follows:

$$g(\omega) = \alpha \int K(z)\eta_0(\omega,z)|E_p(z)|^2 dz, \tag{1}$$

and the detection process can be condensed in the following expression:

$$\Delta r = \beta \left\{ \int p(z)\eta(\omega,z)E_0^2(z)dz + \sum_{m=0}^{2N} (\epsilon_{m-1} - \epsilon_m)u(z_m)(a_m + b_m)^2 \right\}. \tag{2}$$

In these equations α and β are proportionality constants, η_0 are the elastic strain eigenstates, η is the elastic strain in the sample, E the electric field, K is an effective material-dependent generation constant that considers different light-matter couplings, p is the photoelastic constant, g is the spectrum of the generated coherent phonons, and Δr is the laser-induced reflectivity change. In Eq. (2), ϵ_m is the dielectric function of layer m, and z_m is the position of the interface between layers m and $m+1$. The probe field within layer m is $E_0(z) = a_m e^{i\sqrt{\epsilon_m}kz} + b_m e^{-i\sqrt{\epsilon_m}kz}$, and $\sqrt{\epsilon}k$ is the light wave vector. The first term in Eq. (2) is due purely to the photoelastic effect (i.e., a change in the index of refraction induced by strain). The second results from the displacement of the interfaces (i.e., an effective change in the thickness distribution of the cavity). The latter is fully determined by a proper evaluation of the acoustic modes of the structure, and by physical constants (dielectric functions) that are readily available for most materials. The photoelastic constant p, on the other hand, has only been measured for a few materials, and even in those cases for a limited range of wavelengths [26].

We present in Fig. 5 the results of the model for different characteristic situations—namely, discriminating either one of the two detection mechanisms (photoelastic or interface displacement), and localizing the generation process in each one of the materials (Au, GaAs or QDs), setting all other generation constants $K = 0$. For this purpose the QDs' layer has been modeled as a thin (3 nm) homogeneous layer of an average medium. Several conclusions can be drawn from these results: (i) Peaks are calculated to appear, in agreement with experiment, at the frequencies corresponding to confined acoustic Tamm modes, and zone-center vibrations. (ii) Irrespective of the generation material, only with the interface displacement detection mechanism the amplitude of the fundamental breathing mode (19 GHz) relative to the first zone-center vibration (38 GHz) can reproduce the

TABLE I. Generation constants K used in the simulated spectra shown in Fig. 4. All values are referred to K_{GaAs} at room temperature (highlighted in bold). See the text for details.

	K (293 K)	K (80 K)
Au	4	4.25
QDs	0.15	0.6
GaAs	**1**	0.23

experiment; in fact at the used laser energies, far below the GaAs fundamental-gap transition, the interface displacement contribution is expected to prevail because of the relatively small value of the photoelastic constant of GaAs [26,49]. (iii) Concentrating our attention consequently on the interface displacement detection mechanism [panel (b) in Fig. 5], we see that the Au layer and the QDs are the most efficient transducers to generate the confined acoustic Tamm modes; this follows from the strong localization of the associated strain specifically at the surface of the structure. And (iv), for the generation resonant with the QDs the third overtone of the confined acoustic Tamm mode (57 GHz) is significantly more intense than the fundamental one. This follows from the almost perfect localization of the maximum strain associated with the higher overtone specifically at the position of the QDs [see Fig. 1(c)].

Based on these observations we have fitted the measured room temperature spectrum considering the interface displacement detection mechanism, fixing $K_{\mathrm{GaAs}}^{293\,\mathrm{K}} = 1$, and searching for the generation constants at the Au and QD layers so as to better describe the observations. The results are shown with a dashed-dotted curve together with the measured spectrum in Fig. 4 (top), obtained using the fitting parameters given in Table I. The agreement is quite notable almost in every detail, except for an overestimation of the intensity of the higher energy modes. The latter is compatible with the faster anharmonic decay of higher energy vibrations, not accounted for by the calculations [50]. It follows from this fit that at 293 K the off-resonant excitation of the QDs leads to a weak light-sound coupling, while the most efficient transduction occurs at the Au layer. This is reasonable in view of the fact that the absorption of the metallic layer is the main dissipation channel, and thus the related thermal generation mechanisms should be significant.

As follows from the calculations in Fig. 5, one strategy for the more efficient generation of the confined acoustic Tamm modes would be to resonantly couple with the QD optical transition. For this purpose we have performed experiments at 80 K, where the Tamm optical mode overlaps with the broad QD-related absorption. The numerical Fourier transform of the ps acoustic traces is shown in the middle panel of Fig. 4. Again, measured values are displayed with solid curves, calculations with dashed dotted curves. In this case we calculated the thermal stress σ_T at the Au-layer considering the variation of the relevant parameters between 293 and 80 K. That is, $\sigma_T = -3\frac{\beta B Q}{m c_p} \propto \frac{\beta B}{c_p}$, with β the linear expansion coefficient, B the bulk compressibility, Q the amount of heat of the pump laser absorbed by the sample, and c_p the specific heat of the metal at constant pressure. We extracted the values of β, B, and c_p from Refs. [51–53], and obtained that the thermal stress in Au increases 6% when the temperature of the system decreases from room temperature to 80 K. This leads to $K_{\mathrm{Au}}^{80} \sim 4.25$. The generation constants for GaAs and the QDs are then derived from the fit, and given in Table I. The results are physically sound, namely K_{QD} increases by a factor of 4 because of the resonant excitation of the QDs, and K_{GaAs} decreases by a factor of 4, something that is compatible with the blueshift of the band gap by approximately 100 meV. In fact, at the lower temperature the laser gets farther away from the gap, and consequently the associated absorption is reduced thus weakening the deformation potential related generation mechanism.

IV. CONCLUSIONS

In conclusion, we have theoretically analyzed the conditions under which a Tamm plasmon resonator can confine at the same time photons and acoustic vibrations, opening the path to strong optomechanical interactions in these devices. We have shown that indeed resonators designed for the optimum coupling with light, and reportedly used as single-photon emitters, efficient lasers, and cavity polariton devices, result in being optimum for the confinement of vibrations localized in the same region as the Tamm plasmons. The studied devices include a layer of QDs, which can be tuned with the cavity mode to selectively enhance the coherent generation of the Tamm-like confined acoustic vibrations.

The Tamm plasmon resonators are conceptually similar to the GaAs microcavities already reported to evidence very large optomechanical coupling factors. Similar strategies, that is, the use of resonant photoelastic mechanisms and polariton-mediated coupling, could be thus exploited to optimize the optomechanical coupling in the Tamm structures. In addition, photons can be very simply confined in the three dimensions by the use of metal disks instead of planar layers. The same arguments can be used to argue that phonons should also be confined below the metal disks in all directions in such structures. It would be very interesting to study ps acoustics and optomechanical phenomena under these full confinement conditions, for example as a path for the ultrafast efficient modulation of single-photon emitters. As demonstrated here, the maximum strain associated with the third overtone of the fundamental acoustic breathing mode of the Tamm cavities (approximately at 60 GHz) almost perfectly overlaps the location of the maximum electromagnetic field (that is, where the QDs are located).

[1] M. Kaliteevski, I. Iorsh, S. Brand, R. A. Abram, J. M. Chamberlain, A. V. Kavokin, and I. A. Shelykh, Phys. Rev. B **76**, 165415 (2007).

[2] O. Gazzano, S. Michaelis de Vasconcellos, K. Gauthron, C. Symonds, J. Bloch, P. Voisin, J. Bellessa, A. Lemaître, and P. Senellart, Phys. Rev. Lett. **107**, 247402 (2011).

[3] W. L. Zhang and S. F. Yu, Opt. Commun. **283**, 2622 (2010).
[4] C. Symonds, G. Lheureux, J. P. Hugonin, J. J. Greffet, J. Laverdant, G. Brucoli, A. Lemaître, P. Senellart, and J. Bellessa, Nano Lett. **13**, 3179 (2013).
[5] C. Symonds, A. Lemaître, P. Senellart, M. H. Jomaa, S. Aberra Guebrou, E. Homeyer, G. Brucoli, and J. Bellessa, Appl. Phys. Lett. **100**, 121122 (2012).
[6] O. Gazzano, S. Michaelis de Vasconcellos, K. Gauthron, C. Symonds, P. Voisin, J. Bellessa, A. Lemaître, and P. Senellart, Appl. Phys. Lett. **100**, 232111 (2012).
[7] C. Symonds, A. Lemaître, E. Homeyer, J. C. Plenet, and J. Bellessa, Appl. Phys. Lett. **95**, 151114 (2009).
[8] O. Arcizet, P.-F. Cohadon, T. Briant, M. Pinard, and A. Heidmann, Nature (London) **444**, 71 (2006).
[9] T. J. Kippenberg and K. J. Vahala, Science **321**, 1172 (2008).
[10] M. Eichenfield, J. Chan., R. M. Camacho, K. J. Vahala, and O. Painter, Nature (London) **462**, 78 (2009).
[11] M. Aspelmeyer, T. J. Kippenberg, and F. Marquardt, Rev. Mod. Phys. **86**, 1391 (2014).
[12] A. D. O'Connell, M. Hofheinz, M. Ansmann, Radoslaw C. Bialczak, M. Lenander, Erik Lucero, M. Neeley, D. Sank, H. Wang, M. Weides, J. Wenner, John M. Martinis, and A. N. Cleland, Nature (London) **464**, 697 (2010).
[13] J. D. Teufel T. Donner, D. Li, J. W. Harlow, M. S. Allman, K. Cicak, A. J. Sirois, J. D. Whittaker, K. W. Lehnert, and R. W. Simmonds, Nature (London) **475**, 359 (2011).
[14] J. Chan, T. P. Mayer Alegre, A. H. Safavi-Naeini, J. T. Hill, A. Krause, S. Gröblacher, M. Aspelmeyer, and O. Painter, Nature (London) **478**, 89 (2011).
[15] E. Verhagen, S. Deleglise, S. Weis, A. Schliesser, and T. J. Kippenberg, Nature (London) **482**, 63 (2012).
[16] C. Zhao, L. Ju, H. Miao, S. Gras, Y. Fan, and D. G. Blair, Phys. Rev. Lett. **102**, 243902 (2009).
[17] I. S. Grudinin, H. Lee, O. Painter, and K. J. Vahala, Phys. Rev. Lett. **104**, 083901 (2010).
[18] A. Fainstein, B. Jusserand, and V. Thierry-Mieg, Phys. Rev. Lett. **75**, 3764 (1995).
[19] A. Fainstein, B. Jusserand, and V. Thierry-Mieg, Phys. Rev. Lett. **78**, 1576 (1997).
[20] A. Fainstein, B. Jusserand, and V. Thierry-Mieg, Phys. Rev. B **53**, R13287 (1996).
[21] A. Fainstein and B. Jusserand, Phys. Rev. B **57**, 2402 (1998).
[22] N. D. Lanzillotti-Kimura, A. Fainstein, A. Huynh, B. Perrin, B. Jusserand, A. Miard, and A. Lemaître, Phys. Rev. Lett. **99**, 217405 (2007).
[23] Y. Li, Q. Miao, A. V. Nurmikko, and H. J. Maris, J. Appl. Phys. **105**, 083516 (2009).
[24] A. Fainstein, N. D. Lanzillotti-Kimura, B. Jusserand, and B. Perrin, Phys. Rev. Lett. **110**, 037403 (2013).
[25] M. Trigo, A. Bruchhausen, A. Fainstein, B. Jusserand, and V. Thierry-Mieg, Phys. Rev. Lett. **89**, 227402 (2002).
[26] N. Lanzillotti-Kimura, A. Fainstein, and B. Jusserand, Ultrasonics **56**, 80 (2015).
[27] S. Anguiano, G. Rozas, A. E. Bruchhausen, A. Fainstein, B. Jusserand, P. Senellart, and A. Lemaître, Phys. Rev. B **90**, 045314 (2014).
[28] G. Rozas, A. E. Bruchhausen, A. Fainstein, B. Jusserand, and A. Lemaître, Phys. Rev. B **90**, 201302(R) (2014).
[29] M. M. de Lima, Jr., R. Hey, P. V. Santos, and A. Cantarero, Phys. Rev. Lett. **94**, 126805 (2005).
[30] M. M. de Lima, Jr., M. van der Poel, P. V. Santos, and J. M. Hvam, Phys. Rev. Lett. **97**, 045501 (2006); E. A. Cerda-Méndez, D. N. Krizhanovskii, M. Wouters, R. Bradley, K. Biermann, K. Guda, R. Hey, P. V. Santos, D. Sarkar, and M. S. Skolnick, *ibid.* **105**, 116402 (2010).
[31] A. V. Scherbakov, T. Berstermann, A. V. Akimov, D. R. Yakovlev, G. Beaudoin, D. Bajoni, I. Sagnes, J. Bloch, and M. Bayer, Phys. Rev. B **78**, 241302(R) (2008).
[32] T. Berstermann, A. V. Scherbakov, A. V. Akimov, D. R. Yakovlev, N. A. Gippius, B. A. Glavin, I. Sagnes, J. Bloch, and M. Bayer, Phys. Rev. B **80**, 075301 (2009).
[33] T. Czerniuk, C. Brugemann, J. Tepper, S. Brodbeck, C. Schneider, M. Kamp, S. Holing, B. A. Glavin, D. R. Yakovlev, A. V. Akimov, and M. Bayer, Nat. Commun. **5**, 4038 (2014).
[34] T. Czerniuk, J. Tepper, A. V. Akimov, S. Unsleber, C. Schneider, M. Kamp, S. Hoefling, D. R. Yakovlev, and M. Bayer, Appl. Phys. Lett. **106**, 041103 (2015).
[35] A. Fainstein and B. Jusserand, Proc. Int. Conf. Light Scattering Solids, 9th **108**, 17 (2007).
[36] V. Narayanamurti, H. L. Störmer, M. A. Chin, A. C. Gossard, and W. Wiegmann, Phys. Rev. Lett. **43**, 2012 (1979).
[37] N. D. Lanzillotti-Kimura, A. Fainstein, C. A. Balseiro, and B. Jusserand, Phys. Rev. B **75**, 024301 (2007).
[38] A. Soukiassian, W. Tian, D. G. Schlom, N. D. Lanzillotti Kimura, A. Bruchhausen, A. Fainstein, D. A. Tenne, X. X. Xi, H. P. Sun, Xiaoqing Pan, A. Cross, and A. Cantarero, Appl. Phys. Lett. **90**, 042909 (2007).
[39] C. Thomsen, H. T. Grahn, H. J. Maris, and J. Tauc, Phys. Rev. B **34**, 4129 (1986).
[40] A. Bartels, T. Dekorsy, H. Kurz, and K. Kohler, Phys. Rev. Lett. **82**, 1044 (1999).
[41] K. Mizoguchi, M. Hase, S. Nakashima, and M. Nakayama, Phys. Rev. B **60**, 8262 (1999).
[42] O. Matsuda and O. B. Wright, J. Opt. Soc. Am. B **19**, 3028 (2002).
[43] M. F. Pascual Winter, G. Rozas, A. Fainstein, B. Jusserand, B. Perrin, A. Huynh, P. O. Vaccaro, and S. Saravanan, Phys. Rev. Lett. **98**, 265501 (2007).
[44] A. Devos, F. Poinsotte, J. Groenen, O. Dehaese, N. Bertru, and A. Ponchet, Phys. Rev. Lett. **98**, 207402 (2007).
[45] E. Péronne, E. Charron, S. Vincent, S. Sauvage, A. Lemaître, B. Perrin, and B. Jusserand, Appl. Phys. Lett. **102**, 043107 (2013).
[46] N. D. Lanzillotti-Kimura, A. Fainstein, B. Perrin, and B. Jusserand, Phys. Rev. B **84**, 064307 (2011).
[47] N. D. Lanzillotti-Kimura, A. Fainstein, B. Perrin, B. Jusserand, L. Largeau, O. Mauguin, and A. Lemaître, Phys. Rev. B **83**, 201103(R) (2011).
[48] M. F. Pascual-Winter, A. Fainstein, B. Jusserand, B. Perrin, and A. Lemaître, Phys. Rev. B **85**, 235443 (2012).
[49] Christopher Baker, William Hease, Dac-Trung Nguyen, Alessio Andronico, Sara Ducci, Giuseppe Leo, and Ivan Favero, Opt. Express **22**, 14072 (2014).
[50] G. Rozas, M. F. Pascual Winter, B. Jusserand, A. Fainstein, B. Perrin, E. Semenova, and A. Lemaître, Phys. Rev. Lett. **102**, 015502 (2009).
[51] F. C. Nix and D. MacNair, Phys. Rev. **60**, 597 (1941).
[52] J. R. Neighbours and G. A. Alers, Phys. Rev. **111**, 707 (1958).
[53] T. H. Geballe and W. F. Giauque, J. Am. Chem. Soc. **74**, 2368 (1952).